

Article

How an Internal Supramolecular Interaction Determines the Stereochemistry of a Metal Center

 Maxime Steinmetz ¹, Christophe Gourlaouen ²  and David Sémeril ^{1,*} 
¹ Synthèse Organométallique et Catalyse, UMR-CNRS 7177 Institut de Chimie de Strasbourg, Strasbourg University, 67008 Strasbourg, France

² Laboratoire de Chimie Quantique, UMR-CNRS 7177 Institut de Chimie de Strasbourg, Strasbourg University, 67008 Strasbourg, France; gourlaouen@unistra.fr

* Correspondence: dsemeril@unistra.fr; Tel.: +33-(0)3-6885-1550

Abstract: The chloro-*P,N*-(diphenylphosphanyl-[(5-phenyl-1,3,4-oxadiazol-2-ylamino)phenyl-methyl])(*p*-cymene)ruthenium(II) hexafluorophosphate complex (**4**) was obtained in two steps from diphenylphosphanyl-[(5-phenyl-1,3,4-oxadiazol-2-ylamino)phenyl-methyl] borane (**2**). In the first step, the oxadiazole ring coordinated with the ruthenium atom, resulting in the formation of the dichloro-*N*-(diphenylphosphanyl-[(5-phenyl-1,3,4-oxadiazol-2-ylamino)phenyl-methyl]borane)(*p*-cymene) ruthenium(II) complex (**3**). During the crystallization of the *P,N*-chelate ruthenium complex, the formation of conglomerate crystals was revealed by X-ray structure analysis. Only two stereoisomers were obtained with (*S*)-Ru and (*R*)-C configurations in the first complex and with (*R*)-Ru and (*S*)-C configurations in the second. This deracemization during crystallization is due to the formation of a hydrogen bond between the *P,N*-ligand and the chlorine atom (CH•••Cl). This supramolecular interaction allows the transfer of the ligand chirality to the metal center and decrees the stereochemistry of the ruthenium atom.

Keywords: ruthenium; deracemization; conglomerate; hydrogen bond; X-ray analysis



Citation: Steinmetz, M.; Gourlaouen, C.; Sémeril, D. How an Internal Supramolecular Interaction Determines the Stereochemistry of a Metal Center. *Organics* **2024**, *5*, 1–11. <https://doi.org/10.3390/org5010001>

Academic Editor: Tomasz K. Olszewski

Received: 13 October 2023

Revised: 20 November 2023

Accepted: 21 December 2023

Published: 4 January 2024



Copyright: © 2024 by the authors. Licensee MDPI, Basel, Switzerland. This article is an open access article distributed under the terms and conditions of the Creative Commons Attribution (CC BY) license (<https://creativecommons.org/licenses/by/4.0/>).

1. Introduction

Obtaining optically pure compounds is essential since the two enantiomers can have different optical, biological and pharmacological properties. The most infamous example is Thalidomide, a drug prescribed as a sedative or against pregnancy nausea. The active substance has an asymmetric carbon and, therefore, two enantiomers; one has anti-nausea or sedative properties, while the other has proven to be teratogenic and causes malformations during fetal development.

Since Pasteur manually separated, under the microscope with pliers, sodium ammonium tartrate enantiomers through their crystalline form in 1848 [1], several methods have been developed, such as asymmetric synthesis, kinetic resolution of racemates or chiral chromatography [2–5]. For this last possibility, one of the preferred methodologies is asymmetry catalysis [6–8], using, for example, as a chiral agent, phosphines [9–19] or *N*-heterocyclic carbenes [20–22] ligands associated with a transition metal, such as ruthenium [23–27].

Since the pioneering work of Werner on the existence of chiral metal complexes with achiral ligands [28], several half-sandwich ruthenium complexes have been studied [29–31] (Figure 1).

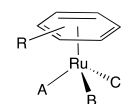


Figure 1. Stereogenic η^6 -arene–ruthenium complex when $A \neq B \neq C$.

We herein describe another example of spontaneous chiral symmetry breaking [32] and deracemization during crystallization [33,34] of η^6 -arene–ruthenium complex. Only two, of the four possible stereoisomers, chiral-at-metal ruthenium complexes were isolated and characterized.

2. Materials and Methods

All synthetic reactions were carried out under an inert atmosphere of argon. Routine ^1H , $^{13}\text{C}\{^1\text{H}\}$, $^{31}\text{P}\{^1\text{H}\}$ and $^{19}\text{F}\{^1\text{H}\}$ spectra were recorded with Bruker FT instruments (AC 300 and 500, Billerica, MA, USA). ^1H , ^{13}C NMR spectroscopic data were referenced to residual chloroform solvents ($\delta = 7.26$ ppm and 77.16 ppm, respectively). ^{19}F and ^{31}P NMR spectroscopic data were given relative to external CCl_3F and H_3PO_4 , respectively. Chemical shifts and coupling constants are labeled in ppm and Hz, respectively. Infrared spectra were recorded with a Bruker FT-IR Alpha-P spectrometer. Mass spectra were recorded on a Bruker MicroTOF spectrometer (ESI-TOF). Elemental analyses were carried out by the Service de Microanalyse, Institut de Chimie, Université de Strasbourg.

Synthesis of diphenylphosphanyl-[(5-phenyl-1,3,4-oxadiazol-2-ylamino)phenyl-methyl]borane (2). In a Schlenk tube, *n*-butyllithium (1.6 M in hexane, 1.20 mL, 1.92 mmol) was rapidly added to a solution of borane–diphenylphosphine complex (400 mg, 2.00 mmol) in THF (50 mL) at -78 °C. After 5 min, the solution was heated to 0 °C, and the reaction mixture was stirred for an additional time of 0.5 h. The generated anion was then cannulated to a solution of (*E*)-1-phenyl-*N*-(5-phenyl-1,3,4-oxadiazol-2-yl) methanimine (1) (496 mg, 1.90 mmol) in THF (50 mL), and the reaction was stirred at room temperature for 16 h. The solution was quenched with water (100 mL), and the aqueous layer was extracted with CH_2Cl_2 (3×50 mL). The combined organic layers were washed with water (2×50 mL) and brine (50 mL), dried over MgSO_4 and filtered. The solvent was then evaporated under reduced pressure, and the crude product was purified by column chromatography (CH_2Cl_2 ; $R_f = 0.22$) to yield compound 2 as a white solid with a 61% yield (520 mg). ^1H NMR (500 MHz, CDCl_3): $\delta = 8.08$ – 8.04 (m, 2H, arom. CH), 7.93 (dd, 2H, arom. CH, $^3J_{\text{HH}} = 7.0$ Hz, $^4J_{\text{HH}} = 2.0$ Hz), 7.67–7.60 (m, 3H, arom. CH), 7.53–7.48 (m, 4H, arom. CH), 7.47–7.42 (m, 3H, arom. CH), 7.36 (td, 2H, arom. CH, $^3J_{\text{HH}} = 7.8$ Hz, $^4J_{\text{HH}} = 2.5$ Hz), 7.30–7.25 (m, 4H, arom. CH), 6.16 (dd, 1H, NH, $^3J_{\text{HH}} = 10.0$ Hz, $^3J_{\text{PH}} = 4.5$ Hz), 6.07 (dd, 1H, CHP, $^2J_{\text{PH}} = 15.0$ Hz, $^3J_{\text{HH}} = 10.0$ Hz), 1.49–0.92 (br s, 3H, BH_3) ppm; $^{13}\text{C}\{^1\text{H}\}$ NMR (126 MHz, CDCl_3): $\delta = 161.88$ (d, arom. Cquat CH(C)PPh₂, $^2J_{\text{CP}} = 11.0$ Hz), 159.90 (s, arom. Cquat C(Ph)=N), 134.17 (d, arom. Cquat C(NH)=N, $^3J_{\text{CP}} = 4.8$ Hz), 133.33 (d, arom. CH of $\text{P}(\text{C}_6\text{H}_5)_2$, $^2J_{\text{CP}} = 8.9$ Hz), 132.75 (d, arom. CH of $\text{P}(\text{C}_6\text{H}_5)_2$, $^2J_{\text{CP}} = 8.9$ Hz), 132.16 (d, arom. CH of $\text{P}(\text{C}_6\text{H}_5)_2$, $^4J_{\text{CP}} = 2.5$ Hz), 131.99 (d, arom. CH of $\text{P}(\text{C}_6\text{H}_5)_2$, $^4J_{\text{CP}} = 2.5$ Hz), 130.92 (s, arom. CH of $\text{C}(\text{C}_6\text{H}_5)=\text{N}$), 129.38 (d, arom. CH of $\text{P}(\text{C}_6\text{H}_5)_2$, $^3J_{\text{CP}} = 10.0$ Hz), 128.98 (s, arom. CH of $\text{C}(\text{C}_6\text{H}_5)=\text{N}$), 128.66 (d, arom. CH of $\text{P}(\text{C}_6\text{H}_5)_2$, $^3J_{\text{CP}} = 10.5$ Hz), 128.58 (d, arom. CH of $\text{CH}(\text{C}_6\text{H}_5)\text{PPh}_2$, $^5J_{\text{CP}} = 2.4$ Hz), 128.52 (d, arom. CH of $\text{CH}(\text{C}_6\text{H}_5)\text{PPh}_2$, $^4J_{\text{CP}} = 3.8$ Hz), 128.18 (d, arom. CH of $\text{CH}(\text{C}_6\text{H}_5)\text{PPh}_2$, $^3J_{\text{CP}} = 1.9$ Hz), 127.43 (d, arom. Cquat of $\text{P}(\text{C}_6\text{H}_5)_2$, $^1J_{\text{CP}} = 81.4$ Hz), 126.16 (d, arom. Cquat of $\text{P}(\text{C}_6\text{H}_5)_2$, $^1J_{\text{CP}} = 77.0$ Hz), 126.04 (s, arom. CH of $\text{C}(\text{C}_6\text{H}_5)=\text{N}$), 124.20 (s, arom. Cquat of $\text{C}(\text{C}_6\text{H}_5)=\text{N}$), 54.06 (d, CHP, $^1J_{\text{CP}} = 41.0$ Hz) ppm; $^{31}\text{P}\{^1\text{H}\}$ NMR (121 MHz, CDCl_3): $\delta = 26.5$ (br s, $\text{P}(\text{BH}_3)\text{Ph}_2$) ppm; IR: $\nu = 1605$ cm^{-1} (C=N). Elemental analysis calculated (%) for $\text{C}_{27}\text{H}_{25}\text{ON}_3\text{PB}$ (449.30): C 72.18, H 5.61, N 9.35; found: C 71.97, H 5.56, N 9.27.

Synthesis of dichloro-*N*-{diphenylphosphanyl-[(5-phenyl-1,3,4-oxadiazol-2-ylamino)phenyl-methyl]borane}(*p*-cymene)ruthenium(II) (3). A solution of phosphanyl borane (2) (0.099 g, 0.22 mmol) in CH_2Cl_2 (50 mL) was added dropwise to a stirred solution of $[\text{RuCl}_2(\textit{p}\text{-cymene})]_2$ (0.067 g, 0.11 mmol) in CH_2Cl_2 (200 mL). The reaction mixture was further stirred at room temperature for 4 h. The solution was then concentrated to ca. 1 mL, upon which *n*-hexane (50 mL) was added. The orange/red precipitate was separated by filtration, washed with hexane (10 mL) and dried under vacuum to yield complex 3 as an orange/red solid with a 92% yield (152 mg). ^1H NMR (500 MHz, CDCl_3): $\delta = 8.47$ (dd, 1H, NH, $^3J_{\text{HH}} = 9.0$ Hz, $^3J_{\text{PH}} = 2.0$ Hz), 7.97–7.93 (m, 2H, arom. CH), 7.88–7.84 (m, 2H,

arom. CH), 7.66–7.64 (m, 2H, arom. CH), 7.52–7.41 (m, 6H, arom. CH), 7.36–7.34 (m, 3H, arom. CH), 7.21–7.16 (m, 5H, arom. CH), 5.61 and 5.31 (AA'BB' spin system, 2H, arom. CH of *p*-cymene, $^3J_{\text{HH}} = 6.5$ Hz, $^4J_{\text{HH}} = 1.5$ Hz), 5.58 and 5.31 (AA'BB' spin system, 2H, arom. CH of *p*-cymene, $^3J_{\text{HH}} = 6.0$ Hz, $^4J_{\text{HH}} = 1.5$ Hz), 5.48 (dd, 1H, arom. CHP, $^2J_{\text{PH}} = 9.2$ Hz, $^3J_{\text{HH}} = 6.5$ Hz), 3.09 (hept, 1H, CH(CH₃)₂, $^3J_{\text{HH}} = 7.0$ Hz), 2.26 (s, 3H, CH₃ of *p*-cymene), 1.29 (d, 3H, CH(CH₃)₂, $^3J_{\text{HH}} = 7.0$ Hz), 1.27 (d, 3H, CH(CH₃)₂, $^3J_{\text{HH}} = 7.0$ Hz), 1.20–0.58 (br s, 3H, BH₃) ppm; $^{13}\text{C}\{^1\text{H}\}$ NMR (126 MHz, CDCl₃): $\delta = 162.03$ (d, arom. Cquat CH(C)PPh₂, $^2J_{\text{CP}} = 4.3$ Hz), 156.51 (s, arom. Cquat C(Ph)=N), 135.03 (d, arom. CH of P(C₆H₅)₂, $^2J_{\text{CP}} = 9.2$ Hz), 134.00 (d, arom. CH of P(C₆H₅)₂, $^2J_{\text{CP}} = 8.9$ Hz), 133.54 (d, arom. Cquat C(NH)=N, $^3J_{\text{CP}} = 1.6$ Hz), 132.25 (d, arom. CH of P(C₆H₅)₂, $^4J_{\text{CP}} = 2.5$ Hz), 131.70 (d, arom. CH of P(C₆H₅)₂, $^4J_{\text{CP}} = 2.5$ Hz), 131.60 (s, arom. CH of C(C₆H₅)=N), 129.13 (s, arom. CH of C(C₆H₅)=N), 128.96 (d, arom. CH of P(C₆H₅)₂, $^3J_{\text{CP}} = 10.2$ Hz), 128.80 (d, arom. CH of P(C₆H₅)₂, $^3J_{\text{CP}} = 10.0$ Hz), 128.63 (d, arom. CH of CH(C₆H₅)PPh₂, $^4J_{\text{CP}} = 4.0$ Hz), 128.45 (d, arom. CH of CH(C₆H₅)PPh₂, $^5J_{\text{CP}} = 2.6$ Hz), 128.05 (d, arom. CH of CH(C₆H₅)PPh₂, $^3J_{\text{CP}} = 2.1$ Hz), 126.25 (d, arom. Cquat of P(C₆H₅)₂, $^1J_{\text{CP}} = 53.5$ Hz), 125.94 (s, arom. CH of C(C₆H₅)=N), 123.23 (d, arom. Cquat of P(C₆H₅)₂, $^1J_{\text{CP}} = 52.5$ Hz), 122.87 (s, arom. Cquat of C(C₆H₅)=N), 102.92 (s, arom. Cquat of *p*-cymene), 98.95 (s, arom. Cquat of *p*-cymene), 84.03 (s, arom. CH of *p*-cymene), 81.35 (s, arom. CH of *p*-cymene), 81.18 (s, arom. CH of *p*-cymene), 59.43 (d, CHP $^1J_{\text{CP}} = 30.1$ Hz), 30.78 (s, CH(CH₃)₂), 22.46 (s, CH(CH₃)₂), 22.32 (s, CH(CH₃)₂), 18.90 (s, CH₃ of *p*-cymene) ppm; $^{31}\text{P}\{^1\text{H}\}$ NMR (121 MHz, CDCl₃): $\delta = 26.1$ (br s, P(BH₃)Ph₂) ppm; IR: $\nu = 1632$ cm⁻¹ (C=N). Elemental analysis calculated (%) for C₃₇H₃₉ON₃PBRuCl₂ (249.27): C 58.82, H 5.20, N 5.56; found: C 58.94, H 5.62, N 5.41.

Synthesis of chloro-*P,N*-{diphenylphosphanyl-[(5-phenyl-1,3,4-oxadiazol-2-ylamino)phenyl-methyl]}(*p*-cymene)ruthenium(II) hexafluorophosphate (4). NaPF₆ (28 mg, 0.17 mmol) was added to a solution of the ruthenium complex 3 (122 mg, 0.16 mmol) in MeOH (100 mL), and the resulting mixture was refluxed for 3.5 h. The reaction was then cooled down to room temperature, concentrated to ca. 40 mL and filtered under celite. The resulting clear solution was evaporated under reduced pressure. The solid was dried under a high vacuum at 40 °C to yield orange/red complex 4 with a 91% yield (137 mg). ^1H NMR (500 MHz, CDCl₃): $\delta = 8.02$ (d, 2H, arom. CH, $^3J_{\text{HH}} = 7.0$ Hz), 7.61–7.49 (m, 11H, arom. CH), 7.40 (td, 2H, arom. CH, $^3J_{\text{HH}} = 7.7$ Hz, $^4J_{\text{HH}} = 3.0$ Hz), 7.18 (td, 1H, arom. CH, $^3J_{\text{HH}} = 7.5$ Hz, $^4J_{\text{HH}} = 1.0$ Hz), 7.03 (t, 2H, arom. CH, $^3J_{\text{HH}} = 7.7$ Hz), 6.69 (d, 2H, arom. CH, $^3J_{\text{HH}} = 7.7$ Hz), 6.43 (d, 1H, CHP, $^2J_{\text{PH}} = 15.5$ Hz), 5.98 (s, 1H, NH), 5.79 and 5.62 (AA'BB' spin system, 2H, arom. CH of *p*-cymene, $^3J_{\text{HH}} = 6.5$ Hz), 5.47 and 5.38 (AA'BB' spin system, 2H, arom. CH of *p*-cymene, $^3J_{\text{HH}} = 6.0$ Hz), 2.46 (hept, 1H, CH(CH₃)₂, $^3J_{\text{HH}} = 6.7$ Hz), 1.90 (s, 3H, CH₃ of *p*-cymene), 1.01 (d, 3H, CH(CH₃)₂, $^3J_{\text{HH}} = 7.0$ Hz), 0.86 (d, 3H, CH(CH₃)₂, $^3J_{\text{HH}} = 6.5$ Hz) ppm; $^{13}\text{C}\{^1\text{H}\}$ NMR (126 MHz, CDCl₃): $\delta = 160.57$ (s, arom. Cquat CH(C)PPh₂), 159.64 (s, arom. Cquat C(Ph)=N), 135.10 (d, arom. CH of P(C₆H₅)₂, $^2J_{\text{CP}} = 9.2$ Hz), 133.77 (d, arom. CH of P(C₆H₅)₂, $^2J_{\text{CP}} = 9.5$ Hz), 132.72 (d, arom. CH of P(C₆H₅)₂, $^4J_{\text{CP}} = 2.8$ Hz), 132.61 (d, arom. CH of P(C₆H₅)₂, $^4J_{\text{CP}} = 2.8$ Hz), 132.49 (s, arom. CH of C(C₆H₅)=N), 131.63 (d, arom. Cquat C(NH)=N, $^3J_{\text{CP}} = 9.2$ Hz), 129.72 (d, arom. CH of CH(C₆H₅)PPh₂, $^5J_{\text{CP}} = 1.8$ Hz), 129.58 (d, arom. CH of P(C₆H₅)₂, $^3J_{\text{CP}} = 10.2$ Hz), 129.36 (s, arom. CH of C(C₆H₅)=N), 129.30 (d, arom. CH of CH(C₆H₅)PPh₂, $^4J_{\text{CP}} = 3.2$ Hz), 128.62 (d, arom. CH of P(C₆H₅)₂, $^3J_{\text{CP}} = 10.3$ Hz), 128.58 (d, arom. CH of CH(C₆H₅)PPh₂, $^3J_{\text{CP}} = 2.1$ Hz), 127.99 (d, arom. Cquat of P(C₆H₅)₂, $^1J_{\text{CP}} = 45.6$ Hz), 126.90 (s, arom. CH of C(C₆H₅)=N), 126.03 (d, arom. Cquat of P(C₆H₅)₂, $^1J_{\text{CP}} = 53.8$ Hz), 122.15 (s, arom. Cquat of C(C₆H₅)=N), 112.32 (s, arom. Cquat of *p*-cymene), 99.80 (s, arom. Cquat of *p*-cymene), 92.27 (d, arom. CH of *p*-cymene, $^2J_{\text{CP}} = 3.2$ Hz), 91.34 (d, arom. CH of *p*-cymene, $^2J_{\text{CP}} = 5.5$ Hz), 91.22 (d, arom. CH of *p*-cymene, $^2J_{\text{CP}} = 3.4$ Hz), 88.61 (d, arom. CH of *p*-cymene, $^2J_{\text{CP}} = 2.4$ Hz), 56.35 (d, CHP, $^1J_{\text{CP}} = 26.2$ Hz), 30.50 (s, CH(CH₃)₂), 22.02 (s, CH(CH₃)₂), 21.53 (s, CH(CH₃)₂), 18.01 (s, CH₃ of *p*-cymene) ppm; $^{31}\text{P}\{^1\text{H}\}$ NMR (121 MHz, CDCl₃): $\delta = 23.4$ (s, PPh₂), -144.3 (hept, PF₆, $^1J_{\text{PF}} = 710.2$ Hz) ppm; $^{19}\text{F}\{^1\text{H}\}$ NMR (282 MHz, CDCl₃): $\delta = -72.77$ (d, PF₆, $^1J_{\text{PF}} = 712.1$ Hz) ppm. IR: $\nu = 1639$ cm⁻¹ (C=N). MS (ESI-TOF):

$m/z = 706.14$ $[M - PF_6]^+$ (expected isotopic profiles). Elemental analysis calculated (%) for $C_{37}H_{36}ON_3P_2F_6RuCl$ (851.17): C 52.21, H 4.26, N 4.94; found: C 52.17, H 4.20, N 4.87.

During the crystallization by slow diffusion of hexane (3.5 mL) into a CH_2Cl_2 solution (0.5 mL) of complex **4** (10 mg), two types of crystals, pack and needles were obtained.

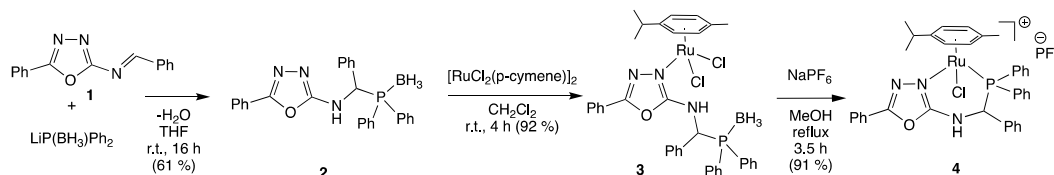
X-ray Crystal Structure Analysis. Single crystals suitable for X-ray analysis were obtained by the slow diffusion of hexane (3.5 mL) into a CH_2Cl_2 solution (0.5 mL) of the compounds (10 mg). The crystals were studied on a Bruker PHOTON-III CPAD (compounds **2**, **3** and **4a**) and Bruker APEX-II CD (complex **4b**), respectively, using Mo- $K\alpha$ radiation ($\lambda = 0.71073 \text{ \AA}$) at $T = 120(2) \text{ K}$. The structures were solved with SHELXT-2014/5 or SHELXT-2018/2 [35], which revealed the non-hydrogen atoms of the molecule. After anisotropic refinement, all of the hydrogen atoms were found with a Fourier difference map. The structure was refined with SHELXL-2014/7, SHELXL-2018/3 or SHELXL-2019/2 [36] by the full-matrix least-square techniques (use of F-square magnitude; x, y, z, bij for C, Ru, B, Cl, F, N, O and P atoms; x, y, z in riding mode for H atoms). Crystal data, data collection and structure refinement details are given in Table 1.

Table 1. Crystal data and structure refinement parameters for compounds **2–4**.

Compound	2	3	4a	4b	
CCDC depository	2296142	2296144	2296150	2296149	
Color	Colorless	Colorless	Orange	Colorless	
Shape	Block	Block	Prism	Plate	
Chemical formula	$C_{27}H_{25}BN_3OP$	$C_{38}H_{41}BCl_4N_3OPRu$	$C_{39}H_{40}Cl_5F_6N_3OP_2Ru$	$C_{75}H_{74}Cl_4F_{12}N_6O_2P_4Ru_2$	
Formula weight (g mol^{-1})	449.28	840.39	1021.00	1787.22	
Crystal system	Triclinic	Triclinic	Triclinic	Triclinic	
Space group	$P-1$	$P-1$	$P1$	$P1$	
Unit cell	a (\AA)	9.9471(5)	11.7923(13)	10.2633(4)	10.430(8)
	b (\AA)	9.9734(5)	12.8299(13)	13.0695(4)	13.135(9)
	c (\AA)	13.1802(7)	14.0024(16)	16.6645(6)	16.931(12)
Parameters	α ($^\circ$)	84.889(2)	81.052(4)	104.9230(10)	104.27(2)
	β ($^\circ$)	69.461(2)	83.206(4)	97.9710(10)	98.05(3)
	γ ($^\circ$)	70.877(2)	65.607(4)	90.0220(10)	90.16(3)
Volume (\AA^3)	1156.38(10)	1902.4(4)	2137.53(13)	2224(3)	
Z	2	2	2	1	
D (g cm^{-3})	1.290	1.467	1.586	1.334	
μ (mm^{-1})	0.144	0.770	0.816	0.600	
T_{\min}, T_{\max}	0.7046, 0.7456	0.887, 0.927	0.867, 0.908	0.931, 0.965	
$F(000)$	472	860	1032	906	
Crystal size (mm)	$0.22 \times 0.14 \times 0.12$	$0.16 \times 0.12 \times 0.10$	$0.18 \times 0.14 \times 0.12$	$0.12 \times 0.08 \times 0.06$	
Index ranges	$-13 \leq h \leq 13$	$-13 \leq h \leq 15$	$-14 \leq h \leq 14$	$-13 \leq h \leq 11$	
	$-13 \leq k \leq 13$	$-16 \leq k \leq 16$	$-18 \leq k \leq 17$	$-17 \leq k \leq 17$	
	$-17 \leq l \leq 17$	$-17 \leq l \leq 18$	$-23 \leq l \leq 23$	$-22 \leq l \leq 22$	
θ range for data collection ($^\circ$)	$2.162 \leq \theta \leq 28.012$	$2.002 \leq \theta \leq 28.087$	$2.218 \leq \theta \leq 30.050$	$1.254 \leq \theta \leq 28.463$	
Reflections collected	40,699	26,123	107,287	44,157	
Independent/observed	5538/5255	8925/6192	22,909/20,812	17,986/9156	
R_{int}	0.0350	0.0692	0.0544	0.1330	
Data/restraints/parameters	5,538/27/368	8,925/9/455	22,909/3/1041	17,986/10/862	
Goodness-of-fit on F^2	1.082	1.053	1.044	0.946	
Final R indices ($I > 2.0 \sigma(I)$)	$R_1 = 0.0804$	$R_1 = 0.1136$	$R_1 = 0.0313$	$R_1 = 0.0765$	
	$wR_2 = 0.2000$	$wR_2 = 0.2540$	$wR_2 = 0.0605$	$wR_2 = 0.1501$	
R indices (all data)	$R_1 = 0.0826$	$R_1 = 0.1583$	$R_1 = 0.0408$	$R_1 = 0.1625$	
	$wR_2 = 0.2010$	$wR_2 = 0.2851$	$wR_2 = 0.0651$	$wR_2 = 0.1875$	
$\Delta\rho_{\max}, \Delta\rho_{\min}$ ($\text{e}\text{\AA}^{-3}$)	0.718, -0.592	2.766, -2.183	0.964, -0.646	0.918, -0.822	

3. Results and Discussion

The synthesis of *P,N*-chelate ruthenium complex **4** required, firstly, the synthesis of diphenylphosphanyl-[(5-phenyl-1,3,4-oxadiazol-2-ylamino)phenyl-methyl]borane **2** (Scheme 1 and Supplementary Materials).



Scheme 1. Synthesis of *P,N*-chelate ruthenium complex **4**.

The ligand (**2**) was obtained via a nucleophilic addition of the lithium phosphido-borane ($\text{LiP}(\text{BH}_3)\text{Ph}_2$) on the (*E*)-1-phenyl-*N*-(5-phenyl-1,3,4-oxadiazol-2-yl) methanimine (**1**) in THF. After purification by column chromatography, compound **2** was obtained as a white solid with a 61% yield. Its structure was established by infrared, multinuclear NMR spectroscopy (^1H , ^{13}C and ^{31}P) and elemental analysis (see Supplementary Materials). The $^{31}\text{P}\{^1\text{H}\}$ NMR spectrum in CDCl_3 displayed a large singlet centered at 26.5 ppm. The ^1H NMR spectrum revealed for the NH and CH(PPh_2) signals two doublets of doublets with a proton/proton ($^3J_{\text{HH}} = 10.0$ Hz) and a phosphorus/proton ($^3J_{\text{PH}} = 4.5$ Hz and $^2J_{\text{PH}} = 15.0$ Hz, respectively) vicinal coupling. The phosphanyl borane **2** crystallizes in the triclinic asymmetric space group *P*-1 (Figure 2). The asymmetric unit was composed of two distinct enantiomeric molecules, in which the C13 atom has an *R* and an *S* configuration. Two phenyl rings (C7–C12 and C16–C21) were disordered over two positions (ratios of 0.5/0.5). The aromatic oxadiazole and its linked phenyl are twisted with a dihedral angle of 22.59° .

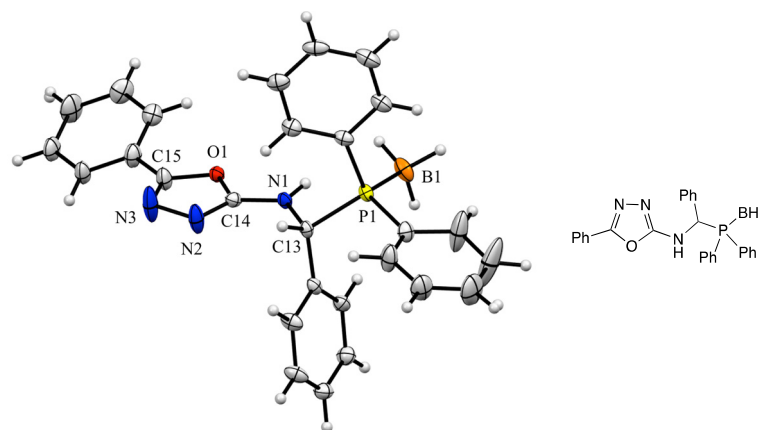


Figure 2. ORTEP drawing of the phosphanyl borane complex **2** (50% probability thermal ellipsoids). Only one of the two molecules present in the unit cell is shown. Important bond lengths (\AA) and angles ($^\circ$): P1–B1 1.924(4), N2–N3 1.423(4), N3–C15 1.280(5), C15–O1 1.372(4), O1–C14 1.361(4), C14–N2 1.290(4), C14–N2–N3 104.8(3), N2–N3–C15 107.1(3), N3–C15–O1 112.3(3), C15–O1–C14 102.2(2), O1–C14–N2 113.7(3).

With phosphanyl borane **2** in hand, its coordination with the $[\text{RuCl}_2(p\text{-cymene})_2]$ precursor via the oxadiazole ring was carried out in dichloromethane. After 4 h at room temperature, the *N*-coordinated ruthenium complex **3** was isolated in 91% yield as an orange/red solid. Formation of the ruthenium complex was deduced from its infrared spectrum, which displayed a shift of the C=N stretching vibrations of the oxadiazole ring from 1605 cm^{-1} in the free ligand **2** to 1632 cm^{-1} in the complex **3** as previously observed for the coordination of oxadiazole moiety to a transition metal [37–40]. The ^1H NMR spectrum reveals the presence of four doublets in the range of 5.31 to 5.61 ppm, attributed

to the four aromatic protons of *p*-cymene ligand, and for the NH proton, an upfield shift of 2.31 ppm with regard to the free ligand **2**. As previously observed, the oxadiazole ring is coordinated to the metal center via its more basic nitrogen atom (noted N1 in Figure 3) [37] as confirmed by its single X-ray diffraction study. The ruthenium complex **3** crystallizes in the triclinic asymmetric space group *P*-1. Two molecules of dichloromethane and two molecules of complexes, in which the C3 atom has an *R* and an *S* configuration, are present in the racemic unit cell. As an attempt, the ruthenium atom adopts a pseudo octahedral geometry, with the *p*-cymene occupying three adjacent sites of the octahedron and a Ru-centroid to *p*-cymene bond length of 1.667 Å. Two chloride atoms are linked to the metal with bond lengths of 2.426 and 2.417 Å. The last site is occupied with the oxadiazole ring of **2** (Ru-N bond length of 2.133 Å). As expected [37], the presence of hydrogen bonds involving the two chlorine atoms and the NH (lengths H3A...Cl1 2.925 and H3A...Cl2 2.558 Å) is observed.

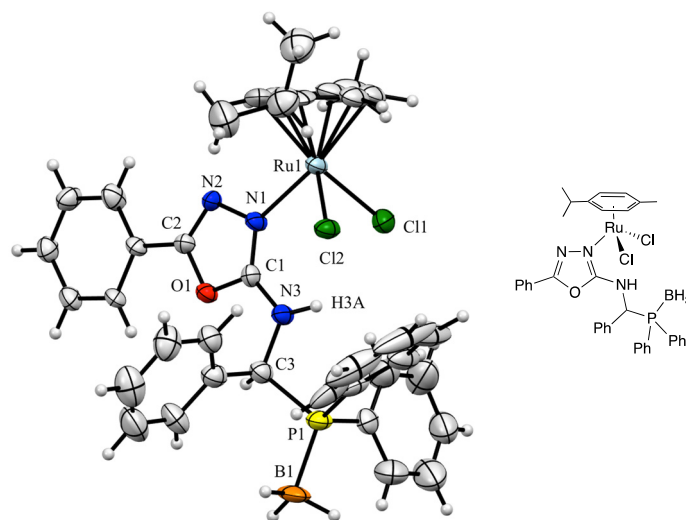


Figure 3. ORTEP drawing of the ruthenium complex **3** (50% probability thermal ellipsoids). Only one of the two complexes present in the unit cell is shown and the two molecules of dichloromethane are not represented. Important bond lengths (Å) and angles (°): P1-B1 1.916 (11), Ru1-Cl1 2.426(3), Ru1-Cl2 2.417(2), Ru1-N1 2.133(6), N1-N2 1.411(9), N2-C2 1.288(10), C2-O1 1.384(10), O1-C1 1.351(9), C1-N1 1.305(11), Cl1-Ru1-N1 85.0(2), Cl1-Ru1-Cl2 87.99(9), Cl2-Ru1-N1 87.3(2), C1-N1-N2 106.5(6), N1-N2-C2 106.1(7), N2-C2-O1 112.3(7), C2-O1-C1 102.9(6), O1-C1-N1 112.2(7).

The formation of the *P,N*-chelate ruthenium **4** was realized by reacting the complex **3** with NaPF₆ in boiling methanol for 3.5 h; under such reaction conditions, deprotection of the phosphane-borane occurred [41]. The desired compound was obtained in 91% isolated yield as an orange/red solid. A mass spectrum of **4** reveals an intense peak at *m/z* = 706.14 corresponding [M – PF₆]⁺ cation with the expected isotopic profile. Consistent with the proposed formula, its infrared spectrum revealed the presence of a coordinated oxadiazole ring ($\nu(\text{C}=\text{N}) = 1639 \text{ cm}^{-1}$) and its ³¹P NMR spectrum displayed a thin singlet at 23.4 ppm. The coordination to the metal center of the *p*-cymene was inferred from the corresponding ¹H NMR spectrum, which shows four doublets in the typical range of 5.38 to 5.79 ppm. More interestingly, examination of NMR spectra revealed two facts: (i) no diastereoisomers are observed; (ii) the NH proton underwent a downfield shift of 2.49 ppm ($\delta = 5.98 \text{ ppm}$) and the CHP proton shifted to higher frequency from 5.48 ppm in complex **3** to 6.43 ppm in complex **4**. These observations suggested that a hydrogen bond involving the chlorine atom and the hydrogen atom of the CHP moiety replaced the previously observed NH...Cl hydrogen bonds of complex **3**, *vide infra*. We observed that for the synthesis of the *P,N*-chelate complex **4**, the coordination order of the two heteroatoms is important. Indeed, it is necessary to coordinate the oxadiazole ring to the metal center in the first step, then in the second step, the phosphorus atom. The reverse order does not lead

to the formation of the desired complex but to a complex mixture of inseparable polymeric compounds.

During the crystallization of the ruthenium complex **4**, two types of crystals, packs **4a** (Figure 4) and needles **4b** (Figure 5), were obtained. Both types of crystals (a pack **4a** and a needle **4b**) were studied by X-ray diffraction. The ruthenium complexes crystallize in the triclinic chiral Sohncke space group *P*1 [42]. Two molecules of complexes are present in the chiral unit cell associated with one and four molecules of dichloromethane for **4b** and **4a**, respectively. The X-ray diffraction studies unambiguously confirmed the formation of *P,N*-chelate ruthenium complexes **4a** and **4b**. The main difference between the solid-state structures concerns the stereochemistry of the ruthenium and the chirality of the *P,N*-ligand. In fact, the two complexes are mirror images of each other and cannot be superimposed, and only two stereoisomers were isolated, complex **4a** with (*S*)-Ru and (*R*)-C configurations (Flack parameter of $-0.015(7)$ [43]) and complex **4b** with (*R*)-Ru and (*S*)-C configurations (Flack parameter of $0.02(4)$).

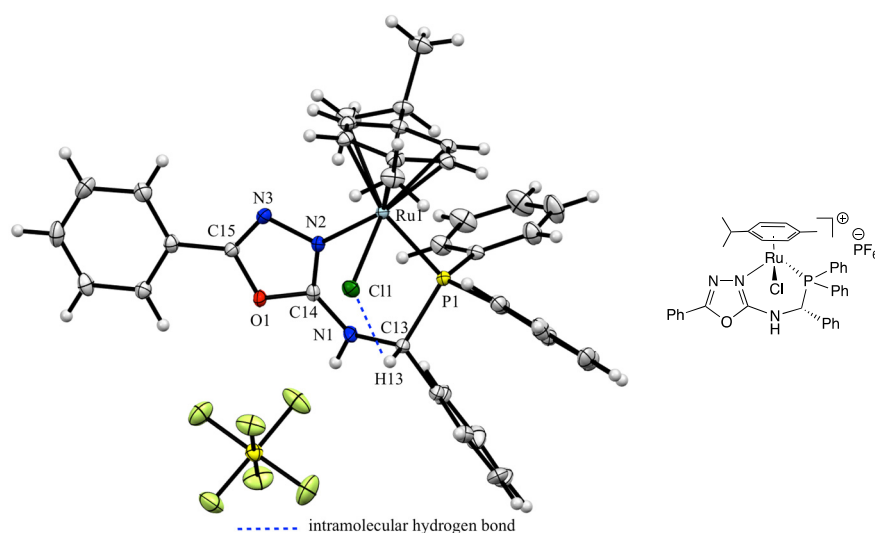


Figure 4. ORTEP drawing of the ruthenium complex **4a** (50% probability thermal ellipsoids). Only one of the two complexes present in the unit cell is shown and the four molecules of dichloromethane are not represented. Important bond lengths (Å) and angles (°): Ru1-Cl1 2.4057(9), Ru1-P1 2.3237(9), Ru1-N2 2.089(3), N2-N3 1.421(4), N3-C15 1.286(4), C15-O1 1.374(4), O1-C14 1.350(4), C14-N2 1.307(4), C14-N1 1.331(5), N1-C13 1.469(4), C13-P1 1.876(3), Cl1-Ru1-N2 82.08(8), Cl1-Ru1-P1 87.00(3), P1-Ru1-N2 86.79(8), C14-N2-N3 107.0(3), N2-N3-C15 105.2(3), N3-C15-O1 112.9(3), C15-O1-C14 103.6(3), O1-C14-N2 111.3(3), Ru1-N2-C14 132.0(2), N2-C14-N1 131.9(3), C14-N1-C13 125.0(3), N1-C13-P1 111.6(2), C13-P1-Ru1 109.60(11).

The molecular structures of complexes **4a** and **4b** exhibit a piano-stool arrangement around the ruthenium atom. The seat was composed of the *p*-cymene ligand (average Ru-centroid of *p*-cymene = 1.716 and 1.736 Å in complexes **4a** and **4b**, respectively) and the three legs by the *P,N*-chelator and a chlorine atom. The bond lengths of Ru1-Cl1 2.4057(9), Ru1-P1 2.3237(9), Ru1-N2 2.089(3), Ru2-Cl2 2.4057(9), Ru2-P2 2.4032(9) and Ru2-N5 2.085(3) Å were observed in complex **4a**. In complex **4b**, the corresponding bond lengths were found to be Ru1-Cl1 2.427(4), Ru1-P1 2.331(4), Ru1-N2 2.090(10), Ru2-Cl2 2.422(4), Ru2-P2 2.341(4) and Ru2-N5 2.086(11) Å. The oxadiazole and phenyl aromatic rings are slightly twisted with dihedral angles of 8.80 and 10.53° in complex **4a** and 5.72 and 9.70° in complex **4b**. In complex **4b**, one PF₆[−] anion has its six fluorine (F1–F6) atoms disordered over two positions with ratios of 0.7/0.3.

In these two complexes, we observe the presence of hydrogen bonds involving the chlorine atom (noted Cl1 in Figures 4 and 5) and the proton of the chiral carbon atom (noted H13 in Figures 4 and 5). The lengths are H13...Cl1 2.715 and H50...Cl2 2.694 Å

in complex **4a** and H13•••Cl1 2.682 and H50•••Cl2 2.698 Å in complex **4b**. Note that for clarity reasons, the atoms labeled H50 and Cl2 belong to the second complex molecule present in the unit cell but are not represented in Figures 4 and 5.

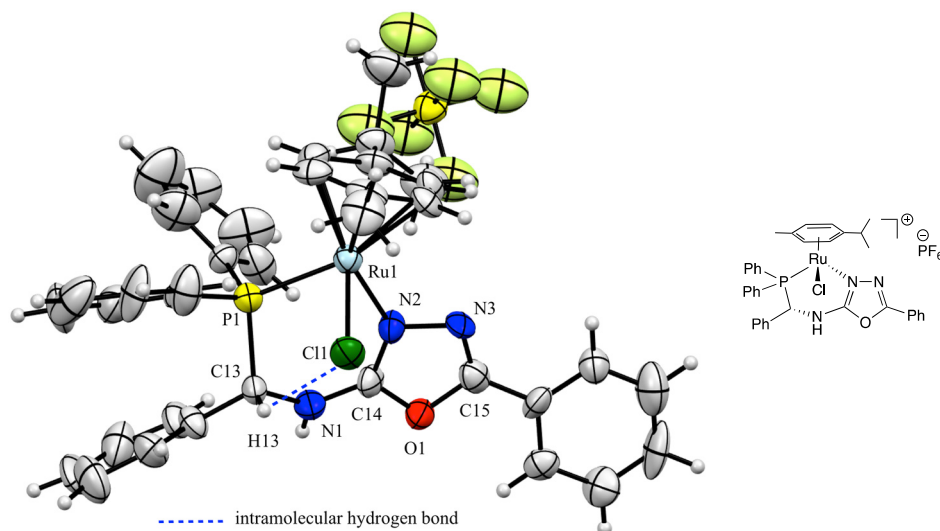


Figure 5. ORTEP drawing of the ruthenium complex **4b** (50% probability thermal ellipsoids). Only one of the two complexes present in the unit cell is shown and the molecule of dichloromethane is not represented. Important bond lengths (Å) and angles (°): Ru1-Cl1 2.427(4), Ru1-P1 2.331(4), Ru1-N2 2.090(10), N2-N3 1.414(14), N3-C15 1.291(17), C15-O1 1.371(15), O1-C14 1.347(14), C14-N2 1.308(16), C14-N1 1.334(15), N1-C13 1.489(15), C13-P1 1.888(13), Cl1-Ru1-N2 82.3(3), Cl1-Ru1-P1 86.99(13), P1-Ru1-N2 86.3(3) C14-N2-N3 107.0(10), N2-N3-C15 105.9(10), N3-C15-O1 111.6(12), C15-O1-C14 104.6(10), O1-C14-N2 110.8(11), Ru1-N2-C14 132.4(9), N2-C14-N1 131.5(12), C14-N1-C13 123.7(11), N1-C13-P1 110.3(9), C13-P1-Ru1 109.0(4).

In each complex, the presence of this hydrogen bond allows a transfer of the chirality of the *P,N*-chelator to the metal and imposes the stereochemistry of the ruthenium atom. Moreover, this supramolecular interaction explains the formation of only two stereoisomers out of the four possible.

The presence of a CH•••Cl hydrogen bond was confirmed by analyzing the noncovalent interaction in the density functional theory optimized structure of the ruthenium complex **4a** (Figure 6 and Figure S21 in Supplementary Materials).

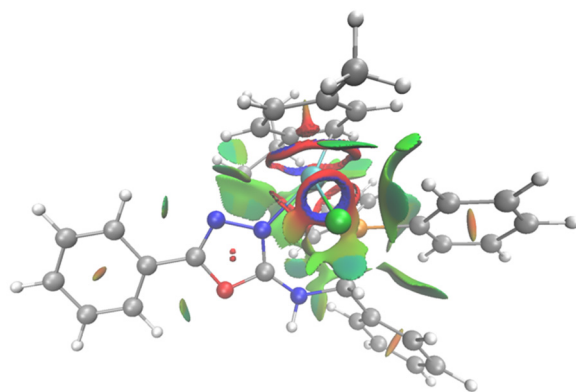


Figure 6. Noncovalent interaction analysis of complexes **4a**. Green areas represent attractive dispersion forces, red areas repulsive steric congestion and blue areas attractive electrostatic interactions.

Furthermore, the calculations reveal that the two experimental structures for complexes **4a** and **4b** are almost degenerate, and the not-observed complexes **5a** (with (*S*)-Ru

and (*S*)-C configurations) and **5b** (with (*R*)-Ru and (*R*)-C configurations) are significantly less stable, around 9.0 kcal/mol (Figure 7).

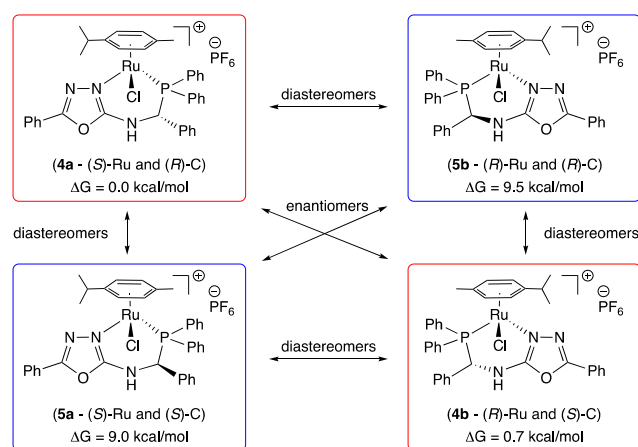


Figure 7. Structures and relative energies of the four diastereomers.

The difference in energy between the four diastereoisomers does not result from the ruthenium coordination sphere distortion as shown by the Ru-X distances (X = Cl, N and P; see Table S1 in Supplementary Materials) almost identical for the four complexes. This difference is the result of (i) the CH...Cl stabilizing inter-ligand interaction (hydrogen bond) present in complexes **4a** and **4b** and absent in complexes **5a** and **5b**; (ii) intra-ligand interactions between the *P,N*-chelate, the *p*-cymene and the chloride anion as illustrated, for example, by the variation in the H-C-C-C dihedral angle of the CH-Ph moiety (see Table S1 in Supplementary Materials). The sum of these interactions increases the stability of the enantiomers **4a** and **4b** compared to the enantiomers **5a** and **5b**.

Finally, it is interesting to note that, in the ^1H NMR spectrum of complex **4**, no vicinal NH-CH ($^3J_{\text{HH}}$) coupling was observed although a small coupling constant between these latter atoms ($\ll 1$ Hz) is present in the COSY experiment. The average H-N-C-H dihedral angles measured in both structures (85.82 and 111.85° in complexes **4a** and **4b**, respectively) confirm the low coupling value.

4. Conclusions

In summary, we have reported the two steps of the synthesis of chloro-*P,N*-{diphenylphosphanyl-[(5-phenyl-1,3,4-oxadiazol-2-ylamino)phenyl-methyl]} (*p*-cymene)ruthenium(II) hexafluorophosphate complex via the initial coordination of the oxadiazole ring to the ruthenium atom and formation of dichloro-*N*-{diphenylphosphanyl-[(5-phenyl-1,3,4-oxadiazol-2-ylamino)phenyl-methyl]borane} (*p*-cymene)ruthenium(II) as intermediate complex. Crystallization of the *P,N*-chelate complex led to the spontaneous formation of conglomerate crystals, which after X-ray structure analysis, revealed the formation of two isomers. In fact, the stereochemistry of the *P,N*-ligand determines that of the ruthenium atom; this transfer of chirality is achieved through a hydrogen bond involving the coordinated chlorine atom. This deracemization during crystallization will be used in future work for the formation of optically active organometallic catalysts, as exemplified by asymmetric hydrogenation.

Supplementary Materials: The following supporting information can be downloaded at <https://www.mdpi.com/article/10.3390/org5010001/s1>. Materials and Methods; synthesis of (*E*)-1-phenyl-*N*-(5-phenyl-1,3,4-oxa-diazol-2-yl) methanimine (**1**) with Figure S1 ^1H NMR spectrum and Figure S2 $^{13}\text{C}\{^1\text{H}\}$ NMR spectrum; characterizing data of diphenylphosphanyl-[(5-phenyl-1,3,4-oxadiazol-2-yl-amino)phenyl-methyl] borane (**2**) with Figure S3 FT-IR spectrum, Figure S4 ^1H NMR spectrum, Figure S5 $^{13}\text{C}\{^1\text{H}\}$ NMR spectrum and Figure S6 $^{31}\text{P}\{^1\text{H}\}$ NMR spectrum; characterizing data of dichloro-*N*-{diphenylphosphanyl-[(5-phenyl-1,3,4-oxadiazol-2-ylamino)phenyl-methyl] borane} (*p*-cymene)ruthenium(II) (**3**) with Figure S7 FT-IR spectrum, Figure S8 ^1H NMR spectrum,

Figure S9 $^{13}\text{C}\{^1\text{H}\}$ NMR spectrum and Figure S10 $^{31}\text{P}\{^1\text{H}\}$ NMR spectrum; characterizing data of chloro-*P,N*-(diphenylphosphanyl)-[(5-phenyl-1,3,4-oxadiazol-2-ylamino)phenyl-methyl] (*p*-cymene) ruthenium(II) hexafluorophosphate (4) with Figure S10 FT-IR spectrum, Figure S12 ^1H NMR spectrum, Figure S13 $^{13}\text{C}\{^1\text{H}\}$ NMR spectrum, Figure S14 $^{19}\text{F}\{^1\text{H}\}$ NMR spectrum, Figure S15 $^{31}\text{P}\{^1\text{H}\}$ NMR spectrum and Figure S16 Mass spectrum (ESI-TOF); Packing pattern in the crystal structure with Figure S17 Packing pattern in the crystal structure of compound 2, Figure S18 Packing pattern in the crystal structure of complex 3, Figure S19 Packing pattern in the crystal structure of complex 4a and Figure S20 Packing pattern in the crystal structure of complex 4b. Computational details with Table S1 Geometrical parameters of the four ruthenium complexes and Figure S21 Non-covalent interaction analysis of complex 5a. Green areas represent attractive dispersion forces, red areas repulsive steric congestion and blue areas attractive electrostatic interactions.

Author Contributions: Conceptualization, D.S.; methodology, M.S., C.G. and D.S.; software, C.G.; validation, C.G. and D.S.; formal analysis, M.S.; investigation, M.S. and C.G.; data curation, M.S., C.G. and D.S.; writing—original draft preparation, M.S., C.G. and D.S.; writing—review and editing, D.S.; visualization, D.S.; supervision, D.S. All authors have read and agreed to the published version of the manuscript.

Funding: This research received no external funding.

Data Availability Statement: The data presented in this study are available upon request from the corresponding authors.

Acknowledgments: M.S. thanks M.R.T. for a research fellowship.

Conflicts of Interest: The authors declare no conflict of interest.

References

1. Flack, H.D. Louis Pasteur's discovery of molecular chirality and spontaneous resolution in 1848, together with a complete review of his crystallographic and chemical work. *Acta Crystallogr. Sect. A* **2009**, *A65*, 371–389. [[CrossRef](#)] [[PubMed](#)]
2. Fogassy, E.; Nógrádi, M.; Kozma, D.; Egri, G.; Pálóvics, E.; Kiss, V. Optical resolution methods. *Org. Biomol. Chem.* **2006**, *4*, 3011–3030. [[CrossRef](#)] [[PubMed](#)]
3. Siedlecka, R. Recent developments in optical resolution. *Tetrahedron* **2013**, *69*, 6331–6363. [[CrossRef](#)]
4. Brill, Z.G.; Condakes, M.L.; Ting, C.P.; Maimone, T.J. Navigating the chiral pool in the total synthesis of complex terpene natural products. *Chem. Rev.* **2017**, *117*, 11753–11795. [[CrossRef](#)]
5. Santos, R.; Pontes, K.V.; Nogueira, I.B.R. Enantiomers and their resolution. *Encyclopedia* **2022**, *2*, 151–188. [[CrossRef](#)]
6. Yoon, T.P.; Jacobsen, E.N. Privileged chiral catalysts. *Science* **2003**, *299*, 1691–1693. [[CrossRef](#)] [[PubMed](#)]
7. Gopalaiah, K. Chiral iron catalysts for asymmetric synthesis. *Chem. Rev.* **2013**, *113*, 3248–3296. [[CrossRef](#)]
8. Shaw, S.; White, J.D. *cis*-2,5-Diaminobicyclo [2.2.2]octane, a new chiral scaffold for asymmetric catalysis. *Acc. Chem. Res.* **2016**, *49*, 1825–1834. [[CrossRef](#)]
9. Barbaro, P.; Bianchini, C.; Giambastiani, G.; Parisel, S.L. Progress in stereoselective catalysis by metal complexes with chiral ferrocenyl phosphines. *Coord. Chem. Rev.* **2004**, *248*, 2131–2150. [[CrossRef](#)]
10. Berthod, M.; Mignani, G.; Woodward, G.; Lemaire, M. Modified BINAP: The how and the why. *Chem. Rev.* **2005**, *105*, 1801–1836. [[CrossRef](#)]
11. Li, Y.-M.; Kwong, F.-Y.; Yu, W.-Y.; Chan, A.S.C. Recent advances in developing new axially chiral phosphine ligands for asymmetric catalysis. *Coord. Chem. Rev.* **2007**, *251*, 2119–2144. [[CrossRef](#)]
12. Xi, J.-H.; Zhou, Q.-L. Chiral diphosphine and monodentate phosphorus ligands on a spiro scaffold for transition-metal-catalyzed asymmetric reactions. *Acc. Chem. Res.* **2008**, *41*, 581–593. [[CrossRef](#)] [[PubMed](#)]
13. Fu, W.; Tang, W. Chiral monophosphorus ligands for asymmetric catalytic reactions. *ACS Catal.* **2016**, *6*, 4814–4858. [[CrossRef](#)]
14. Yanagisawa, A.; Arai, T. Recent advances in chiral phosphine–silver(I) complex-catalyzed asymmetric reactions. *Chem. Commun.* **2008**, *10*, 1165–1172. [[CrossRef](#)]
15. Gual, A.; Godard, C.; Castellón, S.; Claver, C. Highlights of the Rh-catalysed asymmetric hydroformylation of alkenes using phosphorus donor ligands. *Tetrahedron Asymmetry* **2010**, *21*, 1135–1146. [[CrossRef](#)]
16. Wang, T.; Han, X.; Zhong, F.; Yao, W.; Lu, X. Amino acid-derived bifunctional phosphines for enantioselective transformations. *Acc. Chem. Res.* **2016**, *49*, 1369–1378. [[CrossRef](#)]
17. Dutartre, M.; Bayardon, J.; Jugé, S. Applications and stereoselective syntheses of P-chirogenic phosphorus compounds. *Chem. Soc. Rev.* **2016**, *45*, 5771–5794. [[CrossRef](#)] [[PubMed](#)]
18. Chen, X.-S.; Houa, C.-J.; Hu, X.-P. Chiral phosphine-phosphoramidite ligands in asymmetric catalysis. *Synth. Commun.* **2016**, *46*, 917–941. [[CrossRef](#)]
19. Misra, A.; Dwivedi, J.; Kishore, D. Role of the transition metal complexes of 2,2'-bis(diphenylphosphino)-1,1'-binaphthyl (BINAP) in asymmetric catalysis. *Synth. Commun.* **2017**, *47*, 497–535. [[CrossRef](#)]

20. Budagumpi, S.; Keri, R.S.; Achar, G.; Brinda, K.N. Coinage metal complexes of chiral *N*-heterocyclic carbene ligands: Syntheses and applications in asymmetric catalysis. *Adv. Synth. Catal.* **2020**, *362*, 970–997. [[CrossRef](#)]
21. Kong, L.; Morvan, J.; Pichon, D.; Jean, M.; Albalat, M.; Vives, T.; Colombel-Rouen, S.; Giorgi, M.; Dorcet, V.; Roisnel, T.; et al. From prochiral *N*-heterocyclic carbenes to optically pure metal complexes: New opportunities in asymmetric catalysis. *J. Am. Chem. Soc.* **2020**, *142*, 93–98. [[CrossRef](#)] [[PubMed](#)]
22. Jayaraj, A.; Raveedran, A.V.; Latha, A.T.; Priyadarshini, D.; Swamy, P.C.A. Coordination versatility of NHC-metal topologies in asymmetric catalysis: Synthetic insights and recent trends. *Coord. Chem. Rev.* **2023**, *478*, 214922. [[CrossRef](#)]
23. Talavera, G.; Fariña, A.S.; Zanolli-Gerosa, A.; Nedden, H.G. Structural diversity in ruthenium-catalyzed asymmetric transfer hydrogenation reactions. In *Organometallics in Process Chemistry*; Colacot, T.J., Sivakumar, V., Eds.; Topics in Organometallic Chemistry; Springer: Berlin, Germany, 2019; Volume 65, pp. 73–114.
24. Cotman, A.J. Escaping from flatland: Stereoconvergent synthesis of three-dimensional scaffolds via ruthenium(II)-catalyzed Noyori-Ikariya transfer hydrogenation. *Chem. Eur. J.* **2021**, *27*, 39–53. [[CrossRef](#)] [[PubMed](#)]
25. Ortiz, E.; Shezaf, J.Z.; Shen, W.; Krische, M.J. Historical perspective on ruthenium-catalyzed hydrogen transfer and survey of enantioselective hydrogen auto-transfer processes for the conversion of lower alcohols to higher alcohols. *Chem. Sci.* **2022**, *13*, 12625–12633. [[CrossRef](#)]
26. Ritleng, V.; Michon, C. Bidentate donor-functionalized *N*-heterocyclic carbenes: Valuable ligands for ruthenium-catalyzed transfer hydrogenation. *Molecules* **2022**, *27*, 4703. [[CrossRef](#)] [[PubMed](#)]
27. Liang, H.; Wang, J. Enantioselective C–H bond functionalization involving arene ruthenium(II) catalysis. *Chem. Eur. J.* **2023**, *29*, e202202461. [[CrossRef](#)] [[PubMed](#)]
28. Werner, A. Zur Kenntnis des asymmetrischen Kobaltatoms. I. *Ber. Dtsch. Chem. Ges.* **1911**, *44*, 1887–1898. [[CrossRef](#)]
29. Ganter, C. Chiral organometallic half-sandwich complexes with defined metal configuration. *Chem. Soc. Rev.* **2003**, *32*, 130–138. [[CrossRef](#)]
30. Kumar, P.; Gupta, R.K.; Pandey, D.S. Half-sandwich arene ruthenium complexes: Synthetic strategies and relevance in catalysis. *Chem. Soc. Rev.* **2014**, *43*, 707–733. [[CrossRef](#)]
31. Steinlandt, P.S.; Zhang, L.; Meggers, E. Metal stereogenicity in asymmetric transition metal catalysis. *Chem. Rev.* **2023**, *123*, 4764–4794. [[CrossRef](#)]
32. Buhse, T.; Cruz, J.-M.; Noble-Terán, M.E.; Hochberg, D.; Ribó, J.M.; Crusats, J.; Micheau, J.-C. Spontaneous deracemizations. *Chem. Rev.* **2021**, *121*, 2147–2229. [[CrossRef](#)] [[PubMed](#)]
33. Putman, J.I.; Armstrong, D.W. Recent advances in the field of chiral crystallization. *Chirality* **2022**, *34*, 1338–1354. [[CrossRef](#)] [[PubMed](#)]
34. Zhang, B.; Sun, X.; Du, P. Designing single chirality via crystallization method: Spontaneous chiral symmetry breaking and deracemization. *Mater. Today Chem.* **2023**, *32*, 101636. [[CrossRef](#)]
35. Sheldrick, G.M. SHELXT-Integrated space-group and crystal-structure determination. *Acta Crystallogr. Sect. A* **2015**, *A71*, 3–8. [[CrossRef](#)] [[PubMed](#)]
36. Sheldrick, G.M. Crystal structure refinement with SHELXL. *Acta Crystallogr. Sect. C* **2015**, *C71*, 3–8.
37. Hkiri, S.; Gourlaouen, C.; Touil, S.; Samarat, A.; Sémeril, D. 1,3,4-Oxadiazole-functionalized α -amino-phosphonates as ligands for the ruthenium-catalyzed reduction of ketones. *New J. Chem.* **2021**, *45*, 11327. [[CrossRef](#)]
38. Hkiri, S.; Touil, S.; Samarat, A.; Sémeril, D. Functionalized-1,3,4-oxadiazole ligands for the ruthenium-catalyzed Lemieux-Johnson type oxidation of olefins and alkynes in water. *Mol. Catal.* **2022**, *517*, 112014. [[CrossRef](#)]
39. Hkiri, S.; Touil, S.; Samarat, A.; Sémeril, D. Palladium-catalyzed Suzuki–Miyaura cross-coupling with α -aminophosphonates based on 1,3,4-oxadiazole as ligands. *C. R. Chim.* **2022**, *25*, 53–65. [[CrossRef](#)]
40. Hkiri, S.; Coşkun, K.A.; Üstün, E.; Samarat, A.; Tutar, Y.; Şahin, N.; Sémeril, D. Silver(I) complexes based on oxadiazole-functionalized α -aminophosphonate: Synthesis, structural study, and biological activities. *Molecules* **2022**, *27*, 8131. [[CrossRef](#)]
41. Van Overschelde, M.; Verweckena, E.; Modha, S.G.; Cogen, S.; Van der Eycken, E. Catalyst-free alcoholysis of phosphane-boranes: A smooth, cheap, and efficient deprotection procedure. *Tetrahedron* **2009**, *65*, 6410–6415. [[CrossRef](#)]
42. Fecher, G.-H.; Kübler, J.; Felser, C. Chirality in the solid state: Chiral crystal structures in chiral and achiral space groups. *Materials* **2022**, *15*, 5812. [[CrossRef](#)] [[PubMed](#)]
43. Parsons, S.; Flack, H.D.; Wagner, T. Use of intensity quotients and differences in absolute structure refinement. *Acta Crystallogr. Sect. B* **2013**, *B69*, 249–259. [[CrossRef](#)] [[PubMed](#)]

Disclaimer/Publisher’s Note: The statements, opinions and data contained in all publications are solely those of the individual author(s) and contributor(s) and not of MDPI and/or the editor(s). MDPI and/or the editor(s) disclaim responsibility for any injury to people or property resulting from any ideas, methods, instructions or products referred to in the content.